Carbon 215 (2023) 118386

Contents lists available at ScienceDirect

Carbon

journal homepage: www.elsevier.com/locate/carbon

Research article

Graphite rapidly forms via annihilation of screw dislocations

Jacob W. Martin[1], Jason L. Fogg[1], Gabriel R. Francas, Kate J. Putman, Ethan P. Turner, Irene Suarez-Martinez, Nigel A. Marks *

Department of Physics and Astronomy, Curtin University, Bentley, Perth, 6845, WA, Australia

ARTICLE INFO

Keywords:
Graphitization
Molecular dynamics
Disordered carbon
Self-assembly

ABSTRACT

Graphite is the thermodynamically stable form of carbon and yet is remarkably difficult to synthesize. We show the annihilation of screw dislocations is critical for graphitization. These dislocations wind through the layers like a spiral staircase, inhibiting lateral growth of the graphenic crystallites (L_a) and preventing AB stacking of Bernal graphite. High-resolution transmission electron microscopy identifies screws as interdigitated fringes with narrow focal depth in graphitizing polyvinyl chloride. Molecular dynamics simulations of parallel graphenic fragments confirm that screws spontaneously form during heating, with higher annealing temperature driving screw annihilation and crystallite growth. The time evolution and kinetics of graphitization is tracked via X-ray diffraction, showing the growth of L_a and reduction of the interlayer spacing, consistent with screw annihilation. We find that graphite forms orders of magnitude faster than previously assumed, taking less than ten seconds at 3000 °C and just minutes at 2500 °C. This rapid transformation suggests major cost savings in synthetic graphite production, important for lithium-ion batteries and smelting electrodes. By reducing the time spent at ultra-high temperatures, energy costs and component degradation can be significantly lower.

1. Introduction

Graphite plays a vital role in many modern technologies such as lithium-ion batteries, nuclear energy, smelting and graphene production [1–4]. As the world moves towards a greener, decarbonized global economy, the demand for graphite is expected to rise due to the need for batteries to power electric vehicles and store renewable energy [5,6]. Graphite is typically mined from natural deposits, but the purification process can cause environmental impacts due to the acids used and leached metals [1,2]. Synthetic graphite [7] is an attractive alternative but there are two caveats; only a limited set of precursors are available and the graphitization process is energy intensive [2]. Improving our understanding of the graphitization process is crucial to enhance our ability to synthesize graphite and lower the energy requirements of doing so.

The difficulty in manufacturing graphite is surprising, since from a thermodynamics perspective graphite is the most stable form of carbon and yet synthesis requires heat treatment at temperatures exceeding 2500 °C [8]. At such ultra-high temperatures, graphenic fragments rearrange into ordered crystallites during graphitization [9]. Fundamentally, this process centers around the removal of defects. In the early 2000s, Monthioux proposed a classification of defects that are annealed during the graphitization process to allow for graphite formation [10]. Today, it remains unclear which defects belong to this annealable classification [11]. While a number of defects have been shown to inhibit graphite formation, there is no indication of how they relate to Monthioux's classification.

In this work, we show that screw dislocations are the key annealable defects that, when removed, allow graphitization to proceed. This assignment is made possible by a custom pulsed graphite furnace (Fig. 1a,b) that can cycle back and forth between room temperature and 3000 °C in tens of seconds [12,13]. The rapid thermal cycling of our pulsed furnace enables us to produce samples out of equilibrium. In contrast, conventional furnaces take hours to heat and cool [14], meaning recovered samples are always at thermal equilibrium. Using the pulsed furnace, we study graphitization of polyvinyl chloride (PVC) as a function of temperature and time. To achieve time-resolved graphitization we repeatedly heat cycle samples (Fig. 1c) to incrementally step the system towards equilibrium. This technique shows graphitization occurs orders of magnitude faster than previously demonstrated in conventional furnaces [9,15,16].

* Corresponding author.
E-mail address: n.marks@curtin.edu.au (N.A. Marks).
[1] Joint First Authors.

https://doi.org/10.1016/j.carbon.2023.118386
Received 5 June 2023; Received in revised form 17 August 2023; Accepted 21 August 2023
Available online 23 August 2023
0008-6223/© 2023 The Authors. Published by Elsevier Ltd. This is an open access article under the CC BY license (http://creativecommons.org/licenses/by/4.0/).

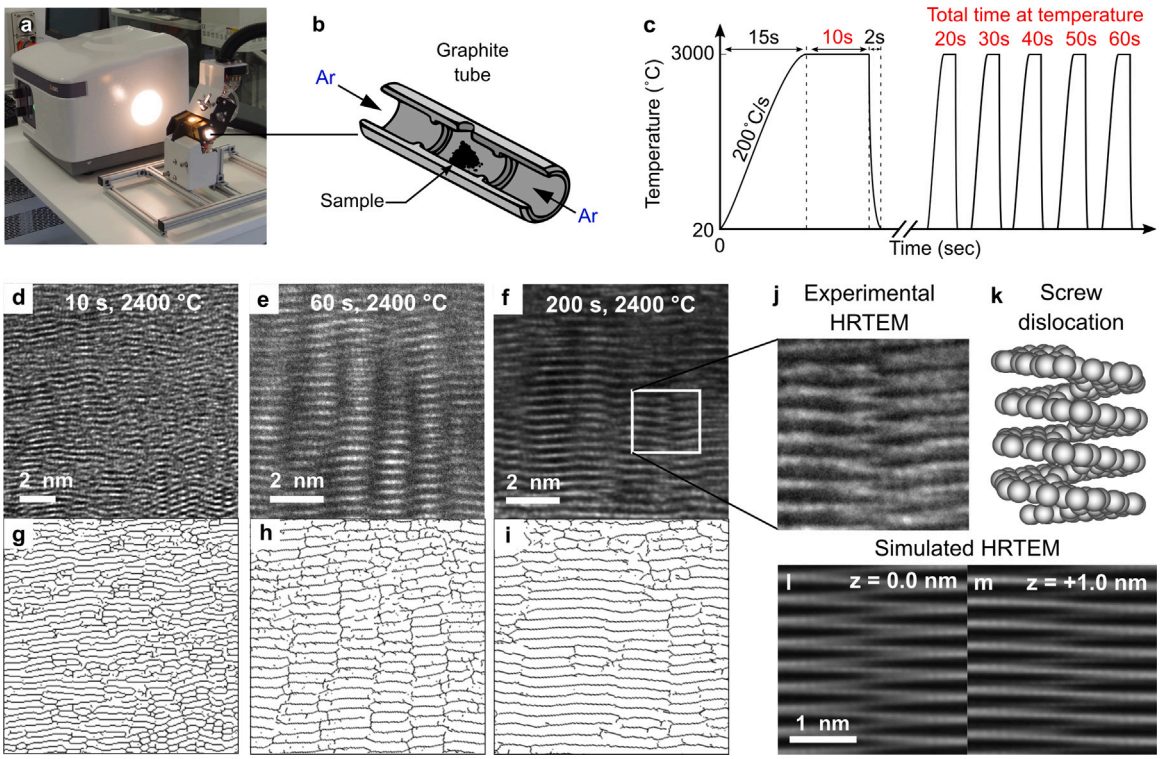

Fig. 1. (a) Custom pulsed graphite furnace in operation. (b) Cross-section of the graphite tube. (c) Temperature profiles used in repeated pulse sequences. (d–f) Phase contrast high-resolution transmission electron microscopy (HRTEM) images for one, six and twenty pulses at 2400 °C. (g–i) Skeletonization of the HRTEM images. (j) Close-up view of a single interdigitated fringe revealing a zig-zag ramped structure. (k) Atomistic model of a screw dislocation in graphite. (l,m) Simulated HRTEM for a screw in AA graphite at focus (z = 0) and at defocus (z = 1 nm).

2. Methodology

2.1. Preparation of carbonized and graphitized samples

PVC is carbonized in a STF 1200 tube furnace, using a ramp rate of 4 °C/min, a hold time of 1 hour at 1000 °C and passive cooling. An inert atmosphere is maintained using argon flowing at a constant 1.5–2 L/min. The carbonized sample is milled in a mortar and pestle before further heating.

Anthracene is carbonized in two stages. First, 11 g of anthracene is rolled in aluminum foil and loaded into a sealed 316 stainless-steel reaction chamber with a volume of 40 ml. The reaction chamber is purged with argon before being heated in a muffle furnace to 500 °C over 1 h and maintaining temperature for a further 6 h. Next, the carbon material is removed from the foil and heated in the STF 1200 furnace over four hours at 1000 °C.

Temperatures above 1000 °C are achieved using a customized furnace built by GBC Scientific Equipment. The system is based on a graphite tube from an atomic absorption spectrometer and is capable of heating to 3000 °C in 1–2 s. Elevated temperatures are maintained for several tens of seconds, while argon gas flows through the tube to prevent combustion. Operation in a pulsed mode extends time at elevated temperature, while a short pause between pulses allows the cooling system to manage the thermal load. Sample size is on the tens of milligrams scale. The temperature profile for heating pulses is as follows: (i) heat from room temperature to 100 °C in 5 s, (ii) ramp to the desired temperature at 200 °C/s, (iii) hold at chosen temperature for 10 s, (iv) cool to room temperature over a few seconds.

2.2. Material characterization

X-ray Diffraction (XRD) is performed in a Bruker D8 Advance Diffractometer with Bragg–Brentano geometry. XRD specimens are prepared by placing a powder sample onto a low-signal silicon wafer holder. Patterns are collected over a 2θ range from 10 to 90° with a dwell time of 1.5 s and step size of 0.3°. Crystallite size (L) is extracted from peak fitting, peak position (θ) and full-width at half-maximum (B), in the standard way via the Scherrer equation:

$$L = \frac{K\lambda}{B\cos\theta}$$

where λ is the wavelength of the incident X-ray beam (1.5406 Å for Cu K-α and 1.7902 Å for Co) and K is the shape factor. For simplicity, we follow the suggestion of Iwashita et al. [17] and use $K = 1$ for both L_a and L_c. The crystallite size in the c-direction (L_c) and the interlayer distance (d_{002}) is computed from the (002) peak, while the crystallite size in the basal plane (L_a) is computed from the (110) peak. Further information on the XRD fitting can be found in Ref. [12].

Transmission electron microscopy (TEM) samples are prepared by grinding with ethanol in an agate mortar. The suspension is sonicated before deposition on 300-mesh lacey carbon grids. Images are collected using a JEOL F200 TEM operating at 200 keV. The instrument is fitted with a cold field emission gun which enables higher-resolution images compared to thermal emission sources. Beam damage is avoided by limiting sample time under the beam and using low beam intensities. Skeletonization is performed based on the methodology developed by Botero et al. [18] but re-implemented in Python with the skimage library [19] and using the thresholding approach from Zack et al. [20].

2.3. Simulations

Screw dislocations for comparison with microscopy images are generated using elastic theory within Atomsk [21]. The atomic coordinates are constructed without periodic boundaries, enabling the representation of a single screw dislocation in AA graphite. The multislice software compuTEM [22] is used to simulate HRTEM images of the dislocations using aberrations matching those of the instrument.

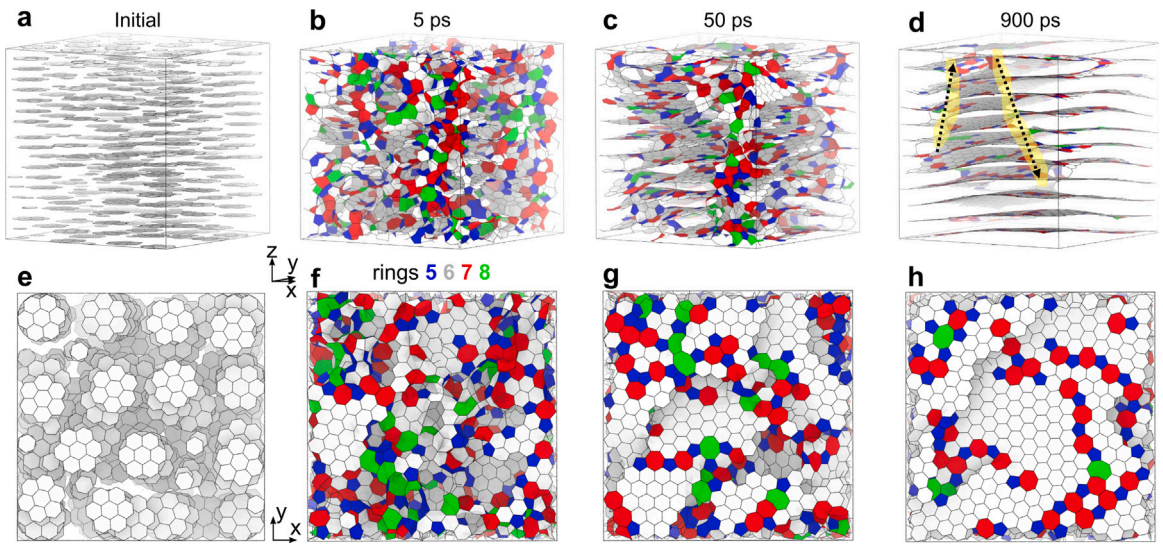

Fig. 2. (a) Initial configuration of aligned hexagonal regions prior to annealing at 3500 K. (b) System after 5 ps, showing loss of original alignment. (c) System after 50 ps, showing the development of graphenic regions. (d) System after 900 ps, showing two screws, highlighted in yellow. Non-hexagonal rings are colored according to ring size. Top row (a–d) is a perspective view along the basal plane, while bottom row (e–h) is a plan view along the *z*-axis. (For interpretation of the references to color in this figure legend, the reader is referred to the web version of this article.)

Molecular Dynamics simulations using periodic boundary conditions are performed as implemented in LAMMPS [23] using the environment dependent interatomic potential for carbon (EDIP) [24,25]. Initial atomic configurations are prepared by packing dehydrogenated coronene with the same orientation into a 4 nm size cube using the software packmol [26]. Dehydrogenated benzene is added until the density reaches 2 g/cc. The initial structure is annealed at 300 K and minimized to allow sufficient crosslinks to form between the fragments before high temperature annealing. Simulations are performed in the NVT ensemble, temperature control is achieved with the Bussi thermostat [27] and a timestep of 0.2 fs is used. Ring statistics are computed using the Franzblau shortest-path ring algorithm [28] as implemented in polypy [29]. A cutoff of 1.85 Å defines a bond. Graphenic regions are geometrically computed based on the connectivity and curvature of hexagonal rings using in-house software described in Ref. [30]. Atomistic structures are rendered using VMD [31].

3. Results and discussion

3.1. Imaging of interlayer defects

HRTEM images in Fig. 1d–f show the time evolution of PVC graphitization at 2400 °C. Fig. 1g–i show the same images processed with a skeletonization algorithm that highlights the dark fringes corresponding to graphenic sheets at the Bragg angle. After a single pulse (Fig. 1d,g), small basic structural units (BSUs) are seen where a few layers locally align, but little long-range ordering is observed. After six pulses (60 s at temperature) the fringes and interlayer defects align into columns extending over many tens of layers (Fig. 1e,h). Skeletonization reveals neighboring columns are out of phase by half an interlayer distance in the *c*-direction, forming an interdigitated texture. For the twenty pulse sample (200 s at temperature), the columns merge into extended fringes, reducing the number of interlayer defects (Fig. 1f,i). These merged fringes are no longer interdigitated but have regions where they bend forming a wrinkled texture, as first noted by Oberlin [9].

We propose that the interdigitated fringes are produced by screw dislocations that connect layers in a helical manner. Fig. 1j shows a close-up view of the interdigitated fringes, revealing features that zig-zag between the layers. The zig-zag feature connects the fringes with ramps that can be seen in an atomistic model of the dislocation core (Fig. 1k). To confirm this proposal we compute HRTEM images of screw dislocations at different focal depths with matching instrumental aberrations. Multislice HRTEM simulations of a single screw in AA graphite at focus (Fig. 1l and Supplementary Fig. 1) reproduce the zig-zag ramp texture, while changing the defocus by 1 nm gives a bent wrinkled texture (Fig. 1m). Supplementary Fig. 2 also shows the wrinkled texture from many screws in AA graphite. This short focal depth is consistent with our experimental observations that changing the defocus by a few nanometres leads to the appearance and disappearance of zig-zags. The beam intensities used during imaging did not lead to any time evolution in the fringes, ruling out beam damage as a source of the interdigitated fringes. Additionally, increasing the beam intensity led to amorphization of the samples rather than promoting graphitization.

With the benefit of hindsight, both interdigitated fringes and screws are present in the literature, albeit at lower resolution. For example, TEM by Oberlin [9] and others [32–34] show textures and general features matching our observations. Screws are a well-known defect in graphite and can be observed on the surface of graphite using optical microscopy, electron microscopy and atomic force microscopy [35,36]. Yakobson et al. even assigned interdigitated fringes to screw dislocations to explain the structure of coal [37]. Leyssale et al. also identified screws in their electron microscopy image-guided atomistic reconstruction (IGAR) model of pyrolytic carbon [38] and irradiated graphite [39]. However, none of these works assigned the defect in the context of graphitization, nor did they study the time dependence at a fixed temperature.

3.2. Screw dislocation formation and removal

To understand how screws form and annihilate we perform molecular dynamics (MD) simulations at high temperature. Fig. 2a shows the initial configuration of graphene fragments (dehydrogenated coronene and benzene) that are parallel to each other but do not form planes. This arrangement mimics the aligned mesophase formed during carbonization of graphitizing carbons [9]. Elevated temperatures of 3500 K are used to enable the dynamics to occur on the nanosecond timescale (see Supplementary Video 1). After 5 ps (Fig. 2b), the fragments fuse forming many non-hexagonal rings, which are colored according to ring number. After 50 ps (Fig. 2c) small stacked regions become visible and extended hexagonal regions develop. By 900 ps (Fig. 2d) several

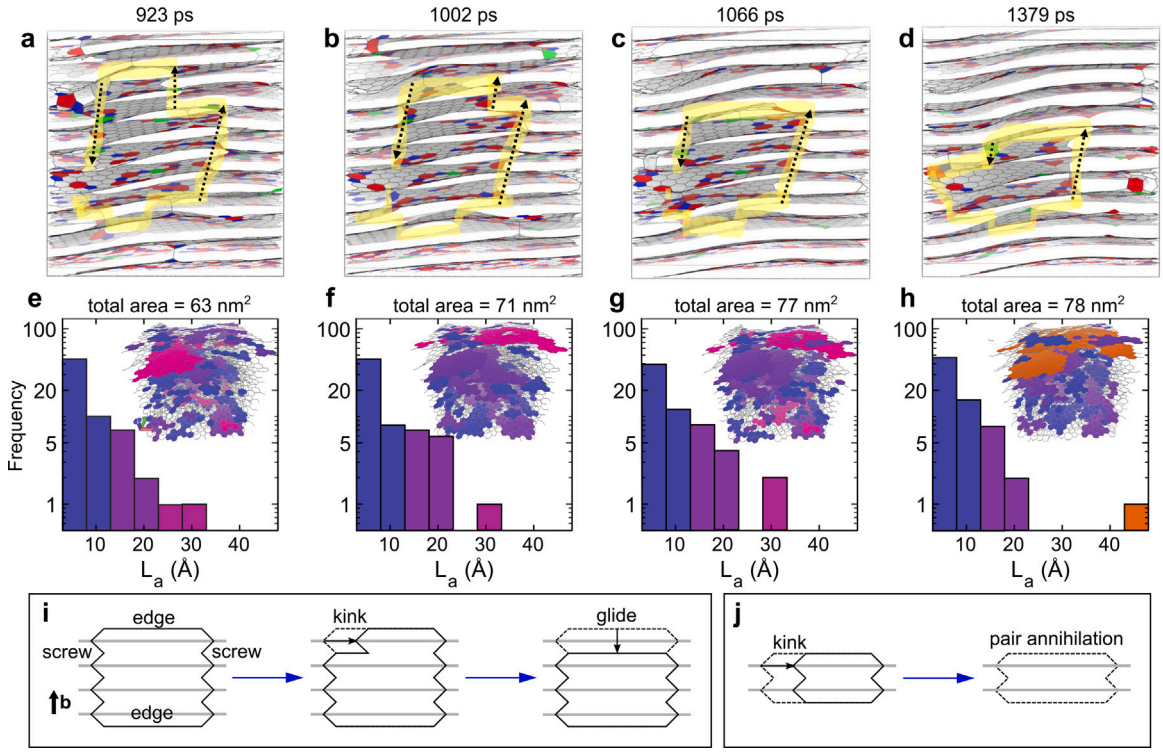

Fig. 3. (a–d) snapshots of slices of the structure during simulations at 3500 K. From (a) to (b) glide motion of the upper edge dislocation reduces the loop height by one layer. Further shrinkage occurs from (b) to (c), and (c) to (d). (e–h) Total area and histograms for the graphenic crystallite size with inset structures colored according to their crystallite sizes. (i) Schematic of the edge glide mechanism for a dislocation loop. (j) Schematic of pair annihilation of the dislocation loop. (For interpretation of the references to color in this figure legend, the reader is referred to the web version of this article.)

screw dislocations are formed and the longest two screws, highlighted in yellow, run over half the length of the simulation cell. The core of the screws is dominated by sp^2 bonded atoms and presents slightly distorted versions of the idealized screw shown in Fig. 1k. These simulations reveal that screws spontaneously form from an ordered precursor, merging the graphenic regions in the mesophase that are parallel but are not coplanar.

Further annealing past 900 ps results in the annihilation of the screw dislocations (see Supplementary Video 2). Fig. 3a-d shows a slice of the system with the dislocation loop highlighted in yellow and the screws marked with an arrow. At the top of Fig. 3a a prismatic edge dislocation can be seen to connect two screws of opposite chirality. As the simulation progresses, the dislocation loop shrinks, increasing the number of perfectly stacked layers. This dislocation loop shrinks through edge gliding which reduces the height of the dislocation loop. A schematic in Fig. 3i shows the mechanism by which the dislocation shrinks: (i) a kink forms at the boundary between the screw and prismatic edge, (ii) the kink migrates along the edge dislocation and (iii) the edge reaches the opposing screw, reducing the height by one layer. Potentially, kinks could initiate from all four corners of the dislocation loop and meet in the middle. Once the dislocation loop has shrunk to two layers, it can annihilate in a process shown schematically in Fig. 3j. The annihilation mechanism involves a kink that propagates along the basal plane, collapsing the edge dislocations together thereby separating the two layers (see Supplementary Fig. 3 for a 3D schematic of how this can occur in AA graphite). We note that some aspects of this final annihilation mechanism have previously been modeled with *ab initio* methods and referred to as a mezzanine defect [40–42].

The growth of graphenic crystallites is tracked in the simulation by considering the hexagonal rings that are connected and closely aligned. Fig. 3e–h show a histogram of the crystallite size, L_a, with insets showing the structure color-coded by fragment size. At the beginning of the time series, a significant fraction of the crystallites are below L_a = 20 Å and there are no large fragments. By the end of the series, the total area of graphenic crystallites has increased from 63 to 78 nm^2 and the fragment distribution contains fewer small fragments and some as large at 50 Å. This growth is facilitated by the annihilation of the screws which enables small fragments to coalesce and form extended sheets.

3.3. Graphitization kinetics

Returning to the experiments, we perform XRD analysis to assess the timescale of graphitization and search for signatures of screw annihilation. Considering first a PVC sample after a single 10 s pulse, Fig. 4a shows the XRD pattern as a function of temperature. At 2000 °C the peaks are broad and the key signatures of Bernal graphite, indicated by the dotted lines, are absent. In contrast, at 3000 °C the pattern shows all the expected features of highly graphitized material, including a sharp (002) reflection, (101) and (112) reflections signifying 3D ordering, and higher order (004) and (006) peaks. Remarkably, just 10 s at this temperature is sufficient to transform the sample into graphite, orders of magnitude faster than conventional furnaces used for synthetic graphite manufacture.

Quantitative analysis of the XRD pattern yields three useful pieces of information, d_{002}, L_c and L_a, all of which are shown in Fig. 4b–d as a function of temperature. At 3000 °C our single pulse heating of PVC and anthracene result in d_{002} values virtually identical to literature values from conventional furnaces. We also see very large values of L_a and L_c consistent with a highly graphitized material. At lower temperatures (circa 2000 °C and below), our d_{002} values are also in close agreement with literature values, indicating that 10 s of heating is sufficient to achieve thermal equilibrium. In the intermediate temperature range, highlighted in grey, our single-pulse data lies above the literature data for PVC and coal tar, indicating that the transformations are kinetically limited. Performing further pulses increases the time at temperature and drives the d_{002} value towards equilibrium (Fig. 4e). After 200 s

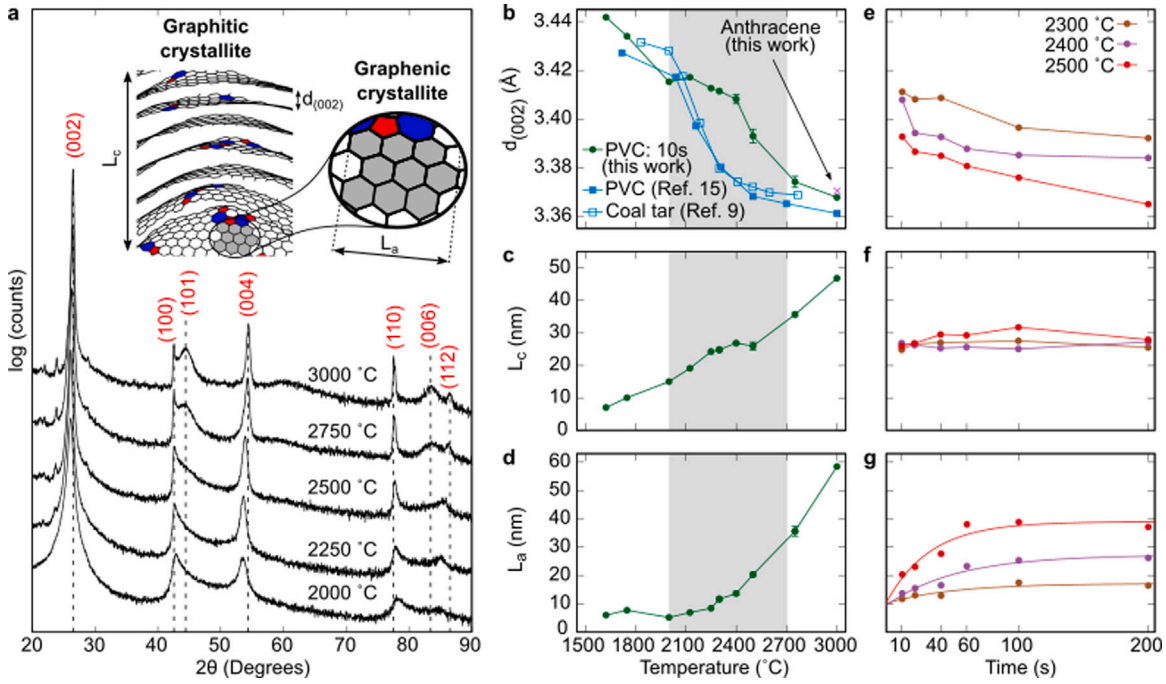

Fig. 4. (a) X-ray pattern for PVC as a function of temperature after a single 10 s pulse. Dotted lines indicate main reflections in perfect graphite. Inset shows a schematic interpretation of the key parameters: L_a, L_c and d_{002}. (b) Interlayer spacing, d_{002}, as a function of temperature. Data from this work (PVC and anthracene) uses a single 10 s pulse. Literature data for PVC from Franklin [15] and coal tar from Oberlin [9] performed in a conventional furnace. Grey region denotes the approximate temperature over which single-pulse data is not at thermal equilibrium. (c) Height of graphitic crystallites, L_c, from this work for PVC after a single 10 s pulse. (d) Size of graphenic crystallites, L_a, from this work for PVC after a single 10 s pulse. (e–g) Time evolution of the three key parameters for PVC after multiple pulses at 2300, 2400 and 2500 °C. Growth in L_a is fitted by an exponential curve to extract rate constants.

(twenty pulses) at 2500 °C the d_{002} value is 3.365 Å, almost identical to the conventional furnace data [9,15]. The work of Ouzilleau et al. [8] provides another way to think about the intermediate region. They analyzed data from conventional furnaces and showed that the d_{002} parameter for all graphitizing carbons follows a universal second-order phase transition with a critical temperature of $T_c = 2280 \pm 50$ °C. We find this critical temperature is shifted to a higher temperature of ~2500 °C for the 10 s pulse but the same profile for d_{002} versus temperature is observed.

The variation in L_c and L_a with time (Fig. 4f-g) are consistent with the annihilation of screws. Removal of this defect increases the lateral (basal) extent of the fragments without changing the number of layers. Both of these trends are seen in the experimental data, with L_c remaining constant and L_a increasing over time towards a plateau value that increases with temperature. The rate of change towards the plateau also varies with temperature, with a more rapid change seen at 2500 °C as compared to 2300 °C. This suggests a thermally activated process that can be quantified using the Arrhenius relationship. The exponential fits in Fig. 4g and an extra dataset at 2250 °C yield an activation barrier of 3.0 ± 1.4 eV (Supplementary Fig. 4). The majority of experiments report activation barriers of 7–11 eV [43], but a few [44–46] report 3.3–4.0 eV, consistent with our work. We note that our value is similar to the energy of a carbon–carbon σ-bond (3.7 eV in diamond [47]) and to the screw migration barrier of 2.8 eV per layer [48] computed using density functional theory.

Removal of screw dislocations explains the progressive reduction of the interlayer distance towards the ideal value of 3.35 Å. Single screw dislocations (Burgers vector of one interlayer distance) only form in AA and ABC graphite, leading to an interlayer distance at the screw core of ~3.5 Å [48]. Since screws inhibit AB stacking they, therefore, provide a plausible explanation for turbostratic graphite in which the graphenic planes are in random registration with an interlayer spacing of 3.42 Å [49]. The screws also provide an assignment for the annealable topological defects discussed by Ouzilleau et al. [11] in the context of graphitizing and non-graphitizing carbons. While their work tentatively suggests a Dienes/Stone–Wales defect [50,51] might be the annealable defect, we propose that screw dislocations provide a better explanation for the variation in d_{002} with temperature.

Screw dislocations could also explain the twisting disorder and magnetic states in graphite [52]. Twisting has been seen as Moiré patterns in both scanning tunneling microscopy and electron microscopy (see Refs. in [53]). In these situations, screws could pin the twisted layers, inhibiting rotation into ideal AB stacking. For small twist angles, exotic magnetic states have been found in twisted bilayer graphene, with a magic angle even enabling a superconducting state [54]. These magnetic states have led to the field of twistronics where 2D layered materials can form useful devices by controlling the twist of their layers. Control of screw defects within carbonaceous materials could potentially enable control of the twist angle and be used for twistronic applications.

From an industrial perspective, an exciting aspect of our work is the potential for significant reductions in the cost of synthetic graphite by reducing electricity usage. Early graphitization studies lead to the consensus that hours were required for graphite synthesis [16], but our experiments show that just minutes are sufficient. Currently, synthetic graphite for electrodes and batteries is produced on the tonnes scale using the Acheson/Castner process in which Joule-heating is applied either directly to the sample (Castner) or to a bed of graphite powder containing the sample (Acheson). Manufacture by these routes is slow, involving half a day to a few days to heat up, an hour at 3000 °C and days to weeks of gradual cooling [55]. The heating stage is highly energy intensive, with electricity consumption of 10–20 MJ/kg [56], similar to steel. Graphite manufacture at the one-kilogram scale uses resistive and induction furnaces to produce highly-oriented pyrolytic graphite (HOPG), rocket nozzles, graphite tiles, etc. In a resistive furnace, a chamber is heated by electricity which in turn emits radiation to heat the sample. Heating takes around an hour, with cooling on the timescale of days to prevent oxidation/combustion of the furnace.

Induction furnaces are a newer technology in which magnetic eddy currents heat the sample, reaching 3000 °C in as little as 15 min for samples at the scale of tens of grams.

The Supplementary Information shows possible graphite manufacturing scenarios in which savings can be made by reducing the time spent at elevated temperatures. Assuming a heat loss proportional to the temperature difference with respect to ambient, the area under the temperature-vs-time heating curve becomes a proxy for electricity cost. In the case of the Acheson/Castner process, reducing the hold time at 3000 °C from an hour to 10 s reduces the power consumption by 40%. Reducing the peak temperature to 2500 °C and holding for 200 s (sufficient to achieve graphite according to Fig. 4e) results in savings of 48%. A lower peak temperature brings a secondary benefit of increasing throughput as cooling times are around 20% less (see Supplementary Information for details). Lower temperatures are also beneficial for resistive furnaces where component degradation sharply increases at high temperatures. Reducing peak temperatures, therefore, results in significant savings in maintenance costs. Our results demonstrate the viability of using induction furnaces to synthesize graphite, and suggest that even faster heating rates might be feasible. For example, reducing the ramping time from 15 to 5 min would reduce electricity costs by two-thirds. Another way to reduce energy costs might be to lower the temperature at which screws move, either using a catalyst (such as silicon) or by applying a mechanical force such as shear (such as present in geological processes).

4. Conclusion

In summary, we study the timescale of graphitization and find that graphite forms much faster than previously thought. Ten seconds at 3000 °C is sufficient for PVC and anthracene to transform into highly graphitic material. At lower temperatures, we track the time evolution and observe that the formation and subsequent annihilation of screw dislocations are a critical step in the graphitization process. The assignment of screws explains historical TEM images and is supported by our atomistic simulations and experimental characterization. Our results impact the synthetic graphite industry by suggesting strategies for reducing electricity and maintenance costs, and increasing throughput.

CRediT authorship contribution statement

Jacob W. Martin: Conceptualization, Methodology, Software, Validation, Investigation, Resources, Writing – original draft, Writing – review & editing, Visualization, Supervision, Project administration. **Jason L. Fogg:** Conceptualization, Methodology, Validation, Formal analysis, Investigation, Data curation, Writing – original draft, Writing – review & editing. **Gabriel R. Francas:** Software, Investigation, Data curation, Visualization. **Kate J. Putman:** Software, Formal analysis, Investigation, Data curation, Visualization. **Ethan P. Turner:** Software, Investigation, Data curation, Visualization. **Irene Suarez-Martinez:** Conceptualization, Methodology, Software, Resources, Writing – original draft, Writing – review & editing, Supervision, Project administration, Funding acquisition. **Nigel A. Marks:** Conceptualization, Methodology, Software, Validation, Formal analysis, Resources, Writing – original draft, Writing – review & editing, Supervision, Project administration, Funding acquisition.

Declaration of competing interest

The authors declare the following financial interests/personal relationships which may be considered as potential competing interests: Jacob W. Martin reports financial support was provided by the Forrest Research Foundation.

Acknowledgments

The authors would like to thank Assoc. Prof. Martin Saunders for his help in collecting the HRTEM images. J.W.M. acknowledges the support of the Forrest Research Foundation. I.S.-M. J.W.M. & N.A.M acknowledges the support of the Australian Research Council (No. FT140100191 & DP190101438). Characterization of the samples were undertaken at the John de Laeter Centre, Curtin University. Computational resources were provided by the Pawsey Centre with funding from the Australian Government and the Government of Western Australia. The authors acknowledge the facilities, and the scientific and technical assistance of Microscopy Australia at the Centre for Microscopy, Characterisation & Analysis, The University of Western Australia, a facility funded by the University, State and Commonwealth Governments.

Appendix A. Supplementary data

Supplementary material related to this article can be found online at https://doi.org/10.1016/j.carbon.2023.118386.

References

[1] L. Zhao, B. Ding, X.-Y. Qin, Z. Wang, W. Lv, Y.-B. He, Q.-H. Yang, F. Kang, Revisiting the roles of natural graphite in ongoing lithium-ion batteries, Adv. Mater. 34 (18) (2022) 2106704.
[2] A.D. Jara, A. Betemariam, G. Woldetinsae, J.Y. Kim, Purification, application and current market trend of natural graphite: A review, Int. J. Mining Sci. Technol. 29 (5) (2019) 671–689.
[3] T. Abram, S. Ion, Generation-IV nuclear power: A review of the state of the science, Energy Policy 36 (12) (2008) 4323–4330.
[4] C. Soldano, A. Mahmood, E. Dujardin, Production, properties and potential of graphene, Carbon 48 (8) (2010) 2127–2150.
[5] D.W. Olson, 2017 Minerals Yearbook - Graphite, United States Geological Survey, 2017.
[6] S. Jaffe, Energy Storage Supply Chain Opportunities, Navigant Research, 2014.
[7] H.O. Pierson, Handbook of Carbon, Graphite, Diamonds and Fullerenes: Processing, Properties and Applications, Noyes Publications, 1993.
[8] P. Ouzilleau, A.E. Gheribi, P. Chartrand, The graphitization temperature threshold analyzed through a second-order structural transformation, Carbon 109 (2016) 896–908.
[9] A. Oberlin, Carbonization and graphitization, Carbon 22 (6) (1984) 521–541, http://dx.doi.org/10.1016/0008-6223(84)90086-1.
[10] M. Monthioux, 4. Structure, texture, and thermal behaviour of polyaromatic solids, in: Carbon Molecules and Materials, CRC Press, 2002, pp. 127–178.
[11] P. Ouzilleau, A.E. Gheribi, P. Chartrand, G. Soucy, M. Monthioux, Why some carbons may or may not graphitize? the point of view of thermodynamics, Carbon 149 (2019) 419–435.
[12] K. Putman, M. Sofianos, M. Rowles, P. Harris, C. Buckley, N. Marks, I. Suarez-Martinez, Pulsed thermal treatment of carbon up to 3000 °C using an atomic absorption spectrometer, Carbon 135 (2018) 157–163, http://dx.doi.org/10.1016/j.carbon.2018.03.060.
[13] J.L. Fogg, K.J. Putman, T. Zhang, Y. Lei, M. Terrones, P.J. Harris, N.A. Marks, I. Suarez-Martinez, Catalysis-free transformation of non-graphitising carbons into highly crystalline graphite, Commun. Mater. 1 (1) (2020) 1–7.
[14] D. Chung, Review graphite, J. Mater. Sci. 37 (8) (2002) 1475–1489.
[15] R.E. Franklin, The structure of graphitic carbons, Acta Crystallogr. 4 (3) (1951) 253–261.
[16] B.T. Kelly, Physics of Graphite, Applied Science Publishers, London, 1981, pp. 1–33, Ch. 1.
[17] N. Iwashita, C.R. Park, H. Fujimoto, M. Shiraishi, M. Inagaki, Specification for a standard procedure of x-ray diffraction measurements on carbon materials, Carbon 42 (2004) 701–714, http://dx.doi.org/10.1016/j.carbon.2004.02.008.
[18] M.L. Botero, Y. Sheng, J. Akroyd, J. Martin, J.A. Dreyer, W. Yang, M. Kraft, Internal structure of soot particles in a diffusion flame, Carbon 141 (2018) 635–642, http://dx.doi.org/10.1016/j.carbon.2018.09.063.
[19] S. Van der Walt, J.L. Schönberger, J. Nunez-Iglesias, F. Boulogne, J.D. Warner, N. Yager, E. Gouillart, T. Yu, Scikit-image: image processing in python, PeerJ 2 (2014) e453.
[20] G.W. Zack, W.E. Rogers, S.A. Latt, Automatic measurement of sister chromatid exchange frequency, J. Histochem. Cytochem. 25 (7) (1977) 741–753.
[21] P. Hirel, Atomsk: A tool for manipulating and converting atomic data files, Comput. Phys. Comm. 197 (2015) 212–219.
[22] E.J. Kirkland, Advanced Computing in Electron Microscopy, Springer US, Boston, MA, 2010, http://dx.doi.org/10.1007/978-1-4419-6533-2.
[23] S. Plimpton, Fast parallel algorithms for short-range molecular dynamics, J. Comput. Phys. 117 (1995) 1–19, http://dx.doi.org/10.1006/jcph.1995.1039.

[24] N.A. Marks, Generalizing the environment-dependent interaction potential for carbon, Phys. Rev. B 63 (3) (2000) 035401, http://dx.doi.org/10.1103/PhysRevB.63.035401.
[25] C. de Tomas, I. Suarez-Martinez, N.A. Marks, Graphitization of amorphous carbons: A comparative study of interatomic potentials, Carbon 109 (2016) 681–693, http://dx.doi.org/10.1016/j.carbon.2016.08.024.
[26] L. Martinez, R. Andrade, E.G. Birgin, J.M. Martínez, PACKMOL: A package for building initial configurations for molecular dynamics simulations, J. Comput. Chem. 30 (13) (2009) 2157–2164, http://dx.doi.org/10.1002/jcc.21224, arXiv:NIHMS150003.
[27] G. Bussi, D. Donadio, M. Parrinello, Canonical sampling through velocity rescaling, J. Chem. Phys. 126 (1) (2007) 014101.
[28] D.S. Franzblau, Computation of ring statistics for network models of solids, Phys. Rev. B 44 (10) (1991) 4925–4930, http://dx.doi.org/10.1103/PhysRevB.44.4925.
[29] J. Kroes, A. Fasolino, G. de Wijs, Graphene Nanoribbons and Edge Reconstructions (Ph.D. thesis), Radboud University Nijmegen, 2010.
[30] K.T. Putman, N.A. Marks, M.R. Rowles, C. de Tomas, J.W. Martin, I. Suarez-Martinez, Defining graphenic crystallites in disordered carbon: moving beyond the platelet model, 2022, arXiv 2. 2212.06354.
[31] W. Humphrey, A. Dalke, K. Schulten, VMD: Visual molecular dynamics, J. Mol. Graph. 14 (1996) 33–38, http://dx.doi.org/10.1016/0263-7855(96)00018-5.
[32] M. Ghazinejad, S. Holmberg, O. Pilloni, L. Oropeza-Ramos, M. Madou, Graphitizing non-graphitizable carbons by stress-induced routes, Sci. Rep. 7 (1) (2017) 1–10, http://dx.doi.org/10.1038/s41598-017-16424-z.
[33] S. Tulić, T. Waitz, M. Čaplovičová, G. Habler, M. Varga, M. Kotlár, V. Vretenár, O. Romanyuk, A. Kromka, B. Rezek, V. Skákalová, Covalent diamond–graphite bonding: Mechanism of catalytic transformation, ACS Nano 13 (4) (2019) 4621–4630.
[34] P.K. Mubari, T. Beguerie, M. Monthioux, E. Weiss-Hortala, A. Nzihou, P. Puech, The x-ray, raman and tem signatures of cellulose-derived carbons explained, C 8 (1) (2022) 4.
[35] G.R. Hennig, Screw dislocations in graphite, Science 147 (3659) (1965) 733–734, http://dx.doi.org/10.1126/science.147.3659.733.
[36] J. Rakovan, J.A. Jaszczak, Multiple length scale growth spirals on metamorphic graphite {001} surfaces studied by atomic force microscopy, Am. Mineral. 87 (1) (2002) 17–24.
[37] Y. Sun, L.B. Alemany, W.E. Billups, J. Lu, B.I. Yakobson, Structural dislocations in anthracite, J. Phys. Chem. Lett. 2 (20) (2011) 2521–2524, http://dx.doi.org/10.1021/jz2011429.
[38] J.-M. Leyssale, J.-P.D. Costa, C. Germain, P. Weisbecker, G.L. Vignoles, Structural features of pyrocarbon atomistic models constructed from transmission electron microscopy images, Carbon 50 (12) (2012) 4388–4400, http://dx.doi.org/10.1016/j.carbon.2012.05.015.
[39] B. Farbos, H. Freeman, T. Hardcastle, J.P.D. Costa, R. Brydson, A.J. Scott, P. Weisbecker, C. Germain, G.L. Vignoles, J.M. Leyssale, A time-dependent atomistic reconstruction of severe irradiation damage and associated property changes in nuclear graphite, Carbon 120 (2017) 111–120, http://dx.doi.org/10.1016/J.CARBON.2017.05.009.
[40] T. Trevethan, P. Dyulgerova, C. Latham, M. Heggie, C. Seabourne, A. Scott, P. Briddon, M. Rayson, Extended interplanar linking in graphite formed from vacancy aggregates, Phys. Rev. Lett. 111 (9) (2013) 095501.
[41] A. Vuong, Nanocarbon: Defect Architectures and Properties (Ph.D. thesis), University of Surrey, United Kingdom, 2017.
[42] A. Vuong, T. Trevethan, C. Latham, C. Ewels, D. Erbahar, P. Briddon, M. Rayson, M. Heggie, Interlayer vacancy defects in aa-stacked bilayer graphene: density functional theory predictions, J. Phys.: Condens. Matter 29 (15) (2017) 155304.
[43] B.T. Kelly, Physics of Graphite, Applied Science Publishers, London, 1981, p. 23, Table 1.3.
[44] T. Noda, M. Inagaki, T. Sekiya, Kinetic studies of the graphitization process—i effect of ambient gas phase on the rate of graphitization, Carbon 3 (2) (1965) 175–180.
[45] A. Tarpinian, C. Tedmon, Wal Tr 851.5/1, Watertown Arsenal Laboratories, 1962.
[46] V. Kasatochkin, A. Kaberov, Dokl. Akad. Nauk SSSR 117 (1957) 837.
[47] H. Shin, S. Kang, J. Koo, H. Lee, J. Kim, Y. Kwon, Cohesion energetics of carbon allotropes: Quantum monte carlo study, J. Chem. Phys. 140 (11) (2014) 114702.
[48] I. Suarez-Martinez, Theory of Diffusion and Plasticity in Layered Carbon Materials (Ph.D. thesis), University of Sussex, 2007.
[49] P. Puech, A. Dabrowska, N. Ratel-Ramond, G.L. Vignoles, M. Monthioux, New insight on carbonisation and graphitisation mechanisms as obtained from a bottom-up analytical approach of x-ray diffraction patterns, Carbon 147 (2019) 602–611.
[50] G.J. Dienes, Mechanism for self-diffusion in graphite, J. Appl. Phys. 23 (11) (1952) 1194–1200.
[51] D.J. Wales, M.A. Miller, T.R. Walsh, Archetypal energy landscapes, Nature 394 (6695) (1998) 758–760, http://dx.doi.org/10.1038/29487.
[52] F.S. Boi, S. Wang, W. Li, O. Odunmbaku, S. Gao, J. Guo, J. Song, J. Wen, H. Zhang, Interplay of edge/screw dislocations and enhanced magnetism in exfoliated pyrolytic graphite with distorted hexagonal moiré superlattices, Carbon Trends 5 (2021) 100106.
[53] J. Campanera, G. Savini, I. Suarez-Martinez, M. Heggie, Density functional calculations on the intricacies of moiré patterns on graphite, Phys. Rev. B 75 (23) (2007) 235449.
[54] Y. Cao, V. Fatemi, S. Fang, K. Watanabe, T. Taniguchi, E. Kaxiras, P. Jarillo-Herrero, Unconventional superconductivity in magic-angle graphene superlattices, Nature 556 (7699) (2018) 43–50.
[55] V. Samoilov, A. Nakhodnova, M. Osmova, D. Verbets, A. Bubnenkov, N. Stepary-ova, A. Gareev, M. Fateeva, D. Shilo, N. Ovsyannikov, Effective heat treatment temperature of carbon materials in high temperature furnaces: Determination by the parameters of raman spectroscopy of witness samples, Inorg. Mater. Appl. Res. 12 (5) (2021) 1416–1427.
[56] J.B. Dunn, L. Gaines, M. Barnes, J.L. Sullivan, M. Wang, Material and Energy Flows in the Materials Production, Assembly, and End-of-Life Stages of the Automotive Lithium-Ion Battery Life Cycle, Tech. rep., Argonne National Lab.(ANL), Argonne, IL (United States), 2014.